Soft Matter

Accepted Manuscript

This is an *Accepted Manuscript*, which has been through the Royal Society of Chemistry peer review process and has been accepted for publication.

Accepted Manuscripts are published online shortly after acceptance, before technical editing, formatting and proof reading. Using this free service, authors can make their results available to the community, in citable form, before we publish the edited article. We will replace this *Accepted Manuscript* with the edited and formatted *Advance Article* as soon as it is available.

You can find more information about *Accepted Manuscripts* in the Information for Authors.

Please note that technical editing may introduce minor changes to the text and/or graphics, which may alter content. The journal's standard Terms & Conditions and the Ethical guidelines still apply. In no event shall the Royal Society of Chemistry be held responsible for any errors or omissions in this *Accepted Manuscript* or any consequences arising from the use of any information it contains.

ROYAL SOCIETY OF CHEMISTRY

www.rsc.org/softmatter

Journal Name

ARTICLE TYPE

Cite this: DOI: 10.1039/xxxxxxxxxx

Microscopic origins of anistropic active stress in motor-driven nematic liquid crystals

Robert Blackwell, Oliver Sweezy-Schindler, Christopher Baldwin, Loren E. Hough, Matthew A. Glaser, and M. D. Betterton

Received Date
Accepted Date

DOI: 10.1039/xxxxxxxxxx

www.rsc.org/journalname

The cytoskeleton, despite comprising relatively few building blocks, drives an impressive variety of cellular phenomena ranging from cell division to motility. These building blocks include filaments, motor proteins, and static crosslinkers. Outside of cells, these same components can form novel materials exhibiting active flows and nonequilibrium contraction or extension. While dipolar extensile or contractile active stresses are common in nematic motor-filament systems, their microscopic origin remains unclear. Here we study a minimal physical model of filaments, crosslinking motors, and static crosslinkers to dissect the microscopic mechanisms of stress generation in a two-dimensional system of orientationally aligned rods. We demonstrate the essential role of filament steric interactions which have not previously be considered to significantly contribute to active stresses. With this insight, we are able to tune contractile or extensile behavior through control of motor-driven filament sliding and crosslinking. This work provides a roadmap for engineering stresses in active liquid crystals. The mechanisms we study may help explain why flowing nematic motor-filament mixtures are extensile while gelled systems are contractile.

1 Introduction

The cellular cytoskeleton drives important biological phenomena including cell migration, cell division, muscle contraction, and organelle transport[1]. Cytoskeletal filaments (actin and myosin), motor proteins (myosins, kinesins, and dynein), and static crosslinkers are also ingredients in synthetic active matter which exhibits new physics such as nonequilibrium self organization and internally generated flows[2–12].

An important challenge to understanding cytoskeletal active matter is to use microscopic interactions between filaments, motors, and crosslinkers to predict macroscopic material properties and dynamics. Experiments on reconstituted systems of stabilized filaments lacking polymerization dynamics, purified motors, and crosslinkers have observed dipolar anisotropic active stresses in orientationally ordered systems. Microtubule-kinesin bundles show extensional motion and extensile flows in a nematic state[10,13,14], while orientationally aligned actin-myosin bundles contract along the bundle axis[8,9,15,16]. Based on these experimental observations and symmetry considerations, dipolar anisotropic active stresses have been incorporated into continuum theories of cytoskeletal active matter[17–22]. However, these phenomenological theories are unable to provide insight into the microscopic origin of active stresses, which remain poorly understood.

The origins of extensile or contractile dipolar stresses are nontrivial because they cannot occur from symmetric pairwise interactions. On antiparallel filaments, motors present on each end of a crosslink tether drive relative filament sliding: when each motor head moves toward the plus end of the filament to which it is bound (fig. 1a), the crosslinking motor exerts forces that separate filament minus ends[23]. If filaments meet at their minus ends, the pair first contracts until the filament midpoints are aligned, and then extends. Symmetric sliding causes no *net* contraction/extension because the initial contraction is balanced by the subsequent extension[24–26]. On parallel filaments, both motors move toward the filament plus ends and no net sliding of the pair occurs[23] (fig. 1b), in the absence of motor pausing at filament ends[24–26] or other motor correlations[27].

Recently we discovered that a minimal physical model of microtubule-motor mixtures generates persistent anisotropic extensile stress in an active nematic liquid crystal phase, using a new computational model of motor binding/unbinding that obeys detailed balance[28]. Here we extend the model to include longer filaments, static crosslinkers, and more general motor force-velocity relations and dissect the origins of active stresses in this system. We find that expectations for stress generation based on consideration of isolated filament pairs are misleading and that insight requires consideration of many-body effects. Although steric in-

Department of Physics, University of Colorado, Boulder, CO 80309

† Electronic Supplementary Information (ESI) available: [details of any supplementary information available should be included here]. See DOI: 10.1039/b000000x/

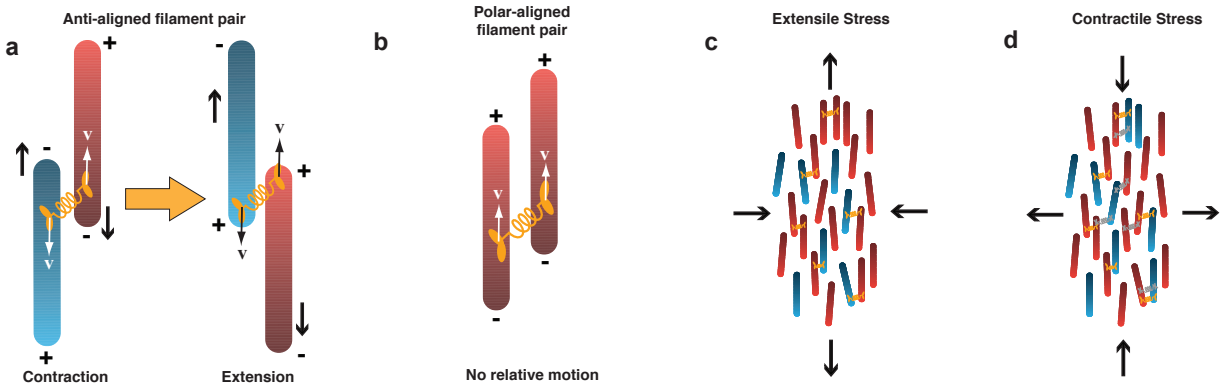

Fig. 1 Overview. In schematics, lighter shading labels filament plus ends and color indicates filament plus-end orientation (red up, blue down. (a) Schematic of motor-driven sliding of polar anti-aligned filaments. Motor heads (orange) move toward filament plus ends, producing forces that slide filaments toward their minus ends. The filament pair initially contracts (left), and then extends (right). (b) Schematic of motor motion on polar-aligned filaments. Motors move toward filament plus ends, producing no relative sliding of the pair. (c) Schematic of motor-driven anisotropic extensile stress in a nematic state. (d) Schematic of motor/crosslink driven anisotropic contractile stress in a nematic state.

teractions between particles play an important role in all liquids, they have so far been neglected in most models of polar filaments driven by crosslinking motors, which consider isolated filament pairs. (We note that the effects of steric interactions on filament alignment have been considered[25,29]).

We find that steric interactions play an important role in active stress generation. Motors slide anti-aligned filaments apart, pushing their minus ends into the ends of other nearby filaments. This increases steric interactions at filament ends relative to filament sides and leads to extensile stress production. We also find extensile stress generation for polar-aligned filament pairs due to motors that are slowed by a retarding force. When a motor walks on a polar-aligned filament pair, the leading head experiences a retarding force and slows its movement. Then the lagging motor is able to catch up, a process which reduces the contractile force sliding the filaments relative to each other. Reduced pair contraction leads to net extensile stress production. With this insight, we can tune our system to change the balance between extensile and contractile stress. Our results suggest that motor properties and degree of fluidity are crucial determinants of extensile versus contractile stress in 2D active liquid crystals.

2 Model

We consider a 2D model of filaments with crosslinkers and motors that drive active motion[28] (fig. 2a). Our goal was to consider a simple physical model able to generate anisotropic active stress. We therefore considered fixed-length, rigid filaments crosslinked and moved by motors, and neglected additional effects such as filament flexibility, motor pausing, and multi-motor bundles, to consider the minimum number of parameters and complexity.

Filaments are rigid polar rods of length l, diameter b, and aspect ratio $r = l/b = 20$. Motors bind, unbind, move toward filament plus ends with a linear force-velocity relation, and exert forces on filaments. Motors bind to two filaments simultaneously with a probability weighted by the Boltzmann factor of the motor extension. To determine the motor unbinding model, we note that some kinesin motors unbind more rapidly with applied force[30], but the crosslinking kinesin-5 motor shows no force-dependent unbinding[31], and myosin motors unbind more slowly with applied force[32]. Here for simplicity we assume motor unbinding is force independent, as was also considered previously[26]. Forces and torques on filaments occur due to motors, short-range steric repulsion, anisotropic local fluid drag by the solvent, and random thermal forces, as discussed below.

Our model differs from previous simulation models of motor-filament systems[33–35] in the treatment of motor/crosslink binding and unbinding: previous work used simple binding rules that do not obey the principle of detailed balance. In our model we accurately calculate the crosslink partition function to ensure that the equilibrium distribution is recovered for static crosslinkers[28]. This improved treatment of the statistical mechanics of motor/crosslink binding and unbinding is important to determine how alterations from equilibrium motor/crosslink distributions occur due to nonequilibrium activity and the resulting active forces generated.

Here we briefly outline the simulation model; further model details are available in previous work[28]. Filaments undergo Brownian dynamics with center-of-mass equations of motion

$$\mathbf{x}_i(t+\delta t) = \mathbf{x}_i(t) + \boldsymbol{\Gamma}_i^{-1}(t)\cdot\mathbf{F}_i(t)\delta t + \delta\mathbf{x}_i(t), \qquad (1)$$

for filaments indexed by i, where the random displacement $\delta\mathbf{x}_i(t)$ is Gaussian-distributed and anisotropic, with variance $\langle\delta\mathbf{x}_i(t)\delta\mathbf{x}_i(t)\rangle = 2k_BT\boldsymbol{\Gamma}_i^{-1}(t)\delta t$, k_B is Boltzmann's constant, T is the absolute temperature, $\mathbf{F}_i(t)$ is the systematic (deterministic) force on filament i and $\boldsymbol{\Gamma}_i^{-1}(t)$ is the inverse friction tensor,

$$\boldsymbol{\Gamma}_i^{-1}(t) = \gamma_\parallel^{-1}\mathbf{u}_i(t)\mathbf{u}_i(t) + \gamma_\perp^{-1}\left[\mathbf{I} - \mathbf{u}_i(t)\mathbf{u}_i(t)\right]. \qquad (2)$$

Here $\gamma_\parallel$ and $\gamma_\perp$ are the parallel and perpendicular drag coefficients of the rod. The equations of motion for filament reorientation are

$$\mathbf{u}_i(t+\delta t) = \mathbf{u}_i(t) + \frac{1}{\gamma_r}\mathbf{T}_i(t)\times\mathbf{u}_i(t)\delta t + \delta\mathbf{u}_i(t), \qquad (3)$$

where γ_r is the rotational drag coefficient, $\mathbf{T}_i(t)$ is the sys-

tematic torque on particle i, and the random reorientation $\delta\mathbf{u}_i(t)$ is Gaussian-distributed, with variance $\langle\delta\mathbf{u}_i(t)\delta\mathbf{u}_i(t)\rangle = 2k_BT/\gamma_r\,[\mathbf{I}-\mathbf{u}_i(t)\mathbf{u}_i(t)]\,\delta t$. To achieve proper dynamics for both long and short filaments, all drag coefficients $\gamma_\perp$, $\gamma_\parallel$, and γ_r were calculated using the method of Löwen et. al[36].

The steric interaction potential between rods is the WCA potential

$$u_{\rm wca}(r_{\rm min}) = \begin{cases} 4k_BT\left[\left(\frac{b}{r_{\rm min}}\right)^{12}-\left(\frac{b}{r_{\rm min}}\right)^{6}\right]+k_BT, & r_{\rm min}<2^{1/6}b \\ 0, & r_{\rm min}\geq 2^{1/6}b, \end{cases} \tag{4}$$

where $r_{\rm min}$ is the minimum distance between the two finite line segments of length l that define the filament axes and b is the effective rod diameter. Note that $r_{\rm min}$ is an implicit function of the center of mass positions and orientations of the two interacting filaments. The typical distance of closest approach between rods is comparable to b, and the thermodynamic properties closely resemble those of hard rods with aspect ratio l/b, a model that is well-characterized both in 2D[37] and 3D[38,39]. We took extra care to prevent unstable overlapping configurations, as discussed previously[28].

Motor- and crosslink-mediated interactions and activity occur in a semi-grand canonical ensemble in which a reservoir of motors is maintained in diffusive contact at a fixed chemical potential $\mu_{\rm m}$ with filaments to/from which they can bind/unbind. Static crosslinkers are treated similarly. The motors are assumed to be noninteracting both in solution and in the bound state, so the motor reservoir can be treated as an ideal solution, and there is no steric interference among bound motors. We assume that, due to the relatively low motor and crosslinker concentrations we study and the availability of multiple surface binding sites on three-dimensional filaments, motors are generally able to avoid steric interactions with each other and with crosslinkers. We therefore neglect steric interations between motors and crosslinkers.

Bound motors have a free energy $u_m(r_m)$, where r_m is the extension of the motor. As in previous work[26], we treat motor attachment (detachment) as a one-step process in which motors bind to (unbind from) two filaments simultaneously, and we assume a binding rate of

$$k_{\rm on}(r) = k_0 e^{-\beta u_m(r)} \tag{5}$$

and an unbinding rate of

$$k_{\rm off}(r) = k_0, \tag{6}$$

where $\beta = (k_BT)^{-1}$ is the inverse temperature in energy units. In contrast to previous work that used simple binding/unbinding rules such as a constant binding rate whenever a motor/crosslink head is within a certain distance of a filament[33–35], this choice of binding and unbinding rates ensures that the correct equilibrium distribution is recovered for static crosslinkers. Given a distribution of motors bound to filaments, we compute the forces and torques exerted on filaments by differentiating $u_m(r_m)$ with respect to the filament positions and orientations.

The endpoints of bound motors translocate toward the plus ends of the filaments to which they are attached with a piecewise linear force-dependent velocity[42] $v = v_0\max(0,\min(1,1+F_\parallel/F_s))$, where the parallel force component $F_\parallel = \mathbf{F}_i\cdot\hat{\mathbf{u}}_i$, v_0 is the maximum translocation velocity, and F_s is the stall force. To keep the model as simple as possible while still capturing the major physics, end pausing of the motors has been excluded. Motors unbind immediately upon reaching the plus end of either of the two filaments to which they are attached. For simulations with both static crosslinkers and motors, bound crosslinkers remain fixed at their attachment sites until they detach according to equation (6). The reversed force-velocity model is identical to the normal motor model except that the motors move faster under load according to the relation $v = v_0\max(1,1-F_\parallel/F_s)$. Motor heads with a force along their direction of motion will move at speed v_0.

To compute the motor/crosslinker binding probability for given filament positions and orientations, we calculate the expected number of motors for each filament pair in the system in equilibrium[28],

$$\langle N_{ij}\rangle = c_m\int_{-l/2}^{l/2}ds_i\int_{-l/2}^{l/2}ds_j\; e^{-\xi_m r_m^2(s_i,s_j)}, \tag{7}$$

where $\xi_m = \beta K_m/2$, K_m is the motor spring stiffness, and the implicit dependence of r_m on filament coordinates has been suppressed. Motors/crosslinkers bind stochastically to the filament pair with a probability proportional to $\langle N_{ij}\rangle$, ensuring that detailed balance is satisfied and the equilibrium distribution is recovered for static crosslinkers and fixed filaments. The average number of motors/crosslinkers that bind to filaments in a time interval δt is

$$\langle N_{\rm a}\rangle = k_0\delta t\,\langle N_{\rm c}\rangle = k_0\delta t\sum_{i<j}^{N}\langle N_{ij}\rangle\,. \tag{8}$$

The number $N_{\rm a}$ of motors/crosslinkers that bind in the interval δt follows a Poisson distribution $\mathscr{P}(N_{\rm a}) = \langle N_{\rm a}\rangle^{N_{\rm a}}e^{-N_{\rm a}}/N_{\rm a}!$ In the kinetic Monte Carlo cycle, the number of bound motors/crosslinkers $N_{\rm a}$ is drawn from this distribution, and $N_{\rm a}$ motors/crosslinkers are inserted by first selecting pairs of filaments with relative probability $\propto\langle N_{ij}\rangle$ and then sampling from the appropriate bivariate normal distribution to choose motor/crosslinker endpoints that lie on the selected pair of filaments.

The overall hybrid Brownian dynamics/kinetic Monte Carlo procedure thus consists of the following steps:

1. Compute forces and torques on filaments, and evolve filament positions and orientations δt forward in time according to the Brownian dynamics equations of motion (Eqs. 1 and 3).

2. Displace each motor endpoint by $v\delta t$ along the filament to which it is attached with translocation velocity v given by the force-velocity relation.

3. Determine the number $N_{\rm d}$ of motors that unbind, and remove this number of motors at random.

4. Compute expected number of bound motors $\langle N_{ij}\rangle$ for all pairs of filaments (Eq. 7) and determine the number $N_{\rm a}$ of motors that bind. Randomly select $N_{\rm a}$ pairs of filaments with

Symbol	Parameter	Value	Notes
k_BT	Thermal energy	4.11×10^{-21} J	Room temperature
l	Filament length	500 nm	Chosen
b	Filament diameter	25 nm	Alberts *et al.* [40]
η	Fluid viscosity	1.0 Pa s	Cytoplasmic viscosity, Wirtz [41]
ρ	Linear density of motor binding sites along filament	–	Appears only in dimensionless concentration.
μ_c	Motor chemical potential	–	Appears only in dimensionless concentration.
u_0	Motor binding free energy	–	Appears only in dimensionless concentration.
v_0	Motor speed (zero force)	Reference 9.0 μm/s, range 0.56–18 μm/s	Of order 1 μm/s, Visscher *et al.* [42]
k_0	Unbinding rate of motors	28.1 s^{-1}	Processivity of 320 nm, Schnitzer *et al.* [30]
f_s	Stall force	1 pN	Visscher *et al.* [42]
K	Motor spring constant	0.013 pN/nm	Decreased from ref Coppin *et al.* [43] to give appropriate range of motor-mediated interaction for zero-equilibrium-length springs

Table 1 Parameters used in simulations.

Symbol	Parameter	Value	Notes
$\phi = N/V(lb+b^2/4)$	Filament packing fraction	0.4157	Chosen to give nematic state at equilibrium in the absence of motors
$r = l/b$	Filament aspect ratio	20	Value for 500-nm MTs
$c = \rho^2 b^2 e^{\beta(\mu_c+u_0)}$	Motor concentration	0.5	Chosen to give average of 2 motors per nearby filament pair
$c_c = \rho^2 b^2 e^{\beta(\mu_c+u_{0,c})}$	Static crosslink concentration (motor and crosslink model)	Reference 0.5, range 0.25–0.5	Chosen to give average of 2 crosslinkers per nearby filament pair
$R_c = \sqrt{k_BT/(Kb^2)}$	Range of motor mediated interaction	$1/\sqrt{2}$	Chosen to be of order 1 for a short-range interaction
$\ell = v_0/(k_0 l)$	Motor run length	Reference 0.64, range 0.04–1.28	Motor-induced active stresses are largest when ℓ is of order 1
$f = f_s b/(k_BT)$	Motor stall force	6	See table 1
$Pe = v_w \eta b/(k_BT)$	Peclet number	Reference 1.358, range 0.085–2.72	Varies with motor speed
$k_{0,m}\tau$	Inverse motor lifetime	1.0	See table 1
$k_{0,c}\tau$	Inverse static crosslink lifetime (motor and crosslink model)	Reference 0.01, range 0.001–1.0	Varied

Table 2 Dimensionless groups used in simulations.

relative probability $\langle N_{ij}\rangle / \sum_{i<j}^{N} \langle N_{ij}\rangle$, and insert a motor between each selected pair of filaments by sampling from a bivariate normal distribution.

5. If system includes static crosslinkers, repeat steps three and four for crosslinkers.

We nondimensionalize using the filament diameter b, the thermal energy k_BT, and the diffusion time τ, defined as the average time for a sphere of diameter b to diffuse $\sqrt{4b^2}$, $\tau = b^2/D$. Then the motor and reversed motor models depend on seven dimensionless parameters: the filament aspect ratio $r = l/b$, the filament packing fraction $\phi = N/V(lb+b^2/4)$, the range of motor mediated interaction $R_m = [k_BT/(Kb^2)]^{1/2}$, the motor concentration $c = z_m \rho^2 b^2 e^{u_0/(k_BT)}$, the motor run length $\ell = v_w/(k_0 l)$, the motor stall force $f = f_s b/(k_BT)$, and the Peclet number (the ratio of translocation and diffusion rates) $Pe = v_w \tau/(3\pi b)$. The motor and static crosslinker model introduces three additional parameters, the range of static crosslinker mediated interaction $R_c = [k_BT/(K_c b^2)]^{1/2}$, the static crosslinker concentration $c_c = z_c \rho^2 b^2 e^{u_{0,c}/(k_BT)}$, and the static crosslinker lifetime $\tau_c = 3\pi/(k_{0,c}\tau)$. Parameter values are summarized in tables 1 and 2.

3 Measurements

To characterize the simulation results, we determined density-density correlations, motor distributions, and active forces for filament pairs in different configurations, as a function of $\mathbf{r}_{ij} = \mathbf{r}_j - \mathbf{r}_i$,

the separation of filaments i and j. The pair distribution function is

$$g(\mathbf{r}) = \frac{V}{N(N-1)} \left\langle \sum_i^N \sum_{j \neq i}^N \delta(\mathbf{r}_{ij} - \mathbf{r}) \right\rangle. \quad (9)$$

The pair distribution function $g(\mathbf{r})$ will typically tend to 1 at infinity for a normal fluid. However, since we often want to observe subsystems of the fluids, such as only polar-aligned pairs, the limiting behavior at infinity is not typically 1 but some smaller fraction. To make comparisons between systems more accessible, we instead study

$$h(\mathbf{r}) = g(\mathbf{r}) - \lim_{\mathbf{r}\to\infty} g(\mathbf{r}) \quad (10)$$

which tends to zero at large distances for all subpopulations. Using this expression, we can easily determine if a system has excess or depleted correlation at a given pair separation by examining the sign of the distribution function $h(\mathbf{r})$.

3.1 Stress and stress anisotropy density

The osmotic stress tensor of a periodic system of N interacting filaments at temperature T in a d-dimensional volume V is given by

$$\boldsymbol{\Sigma} = \frac{N k_B T}{V} \mathbf{I} + \frac{1}{V} \langle \mathbf{W} \rangle, \quad (11)$$

where the first and second terms on the right-hand side represent the ideal gas and interaction contributions, respectively, $\mathbf{I}$ is the unit tensor, and $\mathbf{W}$ is the virial tensor[44],

$$\mathbf{W} = \sum_{i<j}^N \mathbf{r}_{ij} \mathbf{F}_{ij}. \quad (12)$$

where the sum ranges over all interacting pairs of filaments, and $\mathbf{F}_{ij}$ is the force from filament j on filament i. The angular brackets in Eqn. (11) denote an average over time. Here we have assumed that the temperature of the system is isotropic and well-defined, so that

$$\left\langle \sum_{i=1}^N \frac{\mathbf{P}_i \mathbf{P}_i}{m_{\text{fil}}} \right\rangle = \frac{N k_B T}{V} \mathbf{I}, \quad (13)$$

where $\mathbf{P}_i$ is the momentum of filament i and m_{fil} is the filament mass (here assumed the same for all filaments). Filaments have momentum based on their instantaneous movements on short time-scales. This motion is in thermal equilibrium with the background fluid, connecting molecular motion to Brownian motion.

While this relation is clearly true in the equilibrium case, it's less obvious that this relationship holds for active filament/motor systems. However, a purely mechanical definition of osmotic pressure leads to the same expression even for nonequilibrium particle suspensions in the low Reynolds number hydrodynamic regime[45], and we will assume that Eq. (11) holds in the following discussion.

The isotropic pressure is

$$\langle \Pi \rangle = \frac{1}{2} \sum_{j=1}^2 \langle \Sigma_{jj} \rangle, \quad (14)$$

and the average stress anisotropy is

$$\Delta\Sigma = \langle \Sigma_{yy} \rangle - \langle \Sigma_{xx} \rangle, \quad (15)$$

where the y direction corresponds to the instantaneous nematic director orientation and x the perpendicular axis (fig. 2b). The stress anisotropy $\Delta\Sigma = \Sigma_{yy} - \Sigma_{xx}$ is positive for extensile stress and negative for contractile stress. The total stress tensor is determined from all forces between filaments; both elastic forces from crosslinks and steric forces from interfilament repulsion contribute to the stress tensor. For the orientationally aligned systems studied here we typically find anisotropic dipolar stress: if motor activity favors pair extension, then extensile dipolar stress is generated and drives the material to extend in the alignment direction and contract perpendicular to the alignment direction (fig. 1c) and vice versa for pair contraction (fig. 1d) which leads to contractile dipolar stress. In constant-volume simulations, stress anisotropy is unable to relax and can be measured over long runs. In constant-pressure simulations, we adjust the simulation box size to achieve a constant isotropic pressure[44]. Persistent stress anisotropy leads to continuous anisotropic deformation of the simulation box as the system attempts unsuccessfully to reach a constant isotropic pressure.

To characterize how different filament pair configurations contribute to active stress generation, we measured densities of the virial tensor, which we denote $\mathbf{w}(\mathbf{r})$, and the virial stress, which we denote $\boldsymbol{\sigma}_{\text{vir}}(\mathbf{r})$. Both are functions of the filament separation $\mathbf{r}$. The spatial distribution of stress is useful for determining the nature of microscopic stress generation. The virial stress density is

$$\boldsymbol{\sigma}_{\text{vir}}(\mathbf{r}) = \frac{1}{2N(N-1)V} \left\langle \sum_i^N \sum_{j \neq i}^N \delta(\mathbf{r}_{ij} - \mathbf{r}) \mathbf{F}_{ij} \mathbf{r}_{ij} \right\rangle. \quad (16)$$

This density gives the average stress generated by pairs at separation $\mathbf{r}$ and has the property that $\int \boldsymbol{\sigma}_{\text{vir}}(\mathbf{r}) \, \mathrm{d}\mathbf{r} = \boldsymbol{\Sigma}_{\text{vir}}$, the total virial contribution to the stress tensor. We can then define a virial stress anisotropy density by taking the difference in the stress along and perpendicular to the nematic director

$$\Delta\sigma(\mathbf{r}) = \sigma_{\text{vir,yy}}(\mathbf{r}) - \sigma_{\text{vir,xx}}(\mathbf{r}). \quad (17)$$

By integrating the stress anisotropy density along the perpendicular direction (x), we obtain the expression for the 1D stress anisotropy density

$$\Delta\sigma(y) = \int \Delta\sigma_{\text{vir}}(\mathbf{r}) \, \mathrm{d}x. \quad (18)$$

It can also be useful to know the stress contribution for a given configuration without considering contributions due to the pair distribution function. We call this function the configurational virial stress density

$$\boldsymbol{\sigma}_{\text{c}}(\mathbf{r}) = \frac{\boldsymbol{\sigma}_{\text{vir}}(\mathbf{r})}{g(\mathbf{r})} = \frac{1}{2V^2} \frac{\left\langle \sum_i^N \sum_{j \neq i}^N \delta(\mathbf{r}_{ij} - \mathbf{r}) \mathbf{F}_{ij} \mathbf{r}_{ij} \right\rangle}{\left\langle \sum_i^N \sum_{j \neq i}^N \delta(\mathbf{r}_{ij} - \mathbf{r}) \right\rangle} \quad (19)$$

and its corresponding anisotropy measure

$$\Delta\sigma_{\text{c}}(\mathbf{r}) = \Delta\sigma_{\text{c},yy}(\mathbf{r}) - \Delta\sigma_{\text{c},xx}(\mathbf{r}). \quad (20)$$

We also defined a pair normalized virial anisotropy density $\Delta \mathrm{w}_{\mathrm{pair}}(y)$. Due to the tendency of active nematics to form polar domains, the number of polar-aligned pairs outnumbers the number of anti-aligned pairs in a typical simulation by approximately ten to one. This difference makes comparing the stress contributions from the polar-aligned and anti-aligned subsystems difficult when considering the absolute magnitude of stress contributions alone. In order to make quantitative comparisons of the two subsystems with a properly intensive property, we normalized the virial density $\mathbf{w}(\mathbf{r})$ by the number of total interacting pairs for each given subsystem. We defined an interacting pair as a pair where the expected number of attached motors in equilibrium was greater than the threshold $N_{\mathrm{c}} = 10^{-3}$. The virial stress density per filament pair is

$$\mathbf{w}_{\mathrm{pair}}(\mathbf{r}) = \frac{\sum_i^N \sum_{j\neq i} \delta(\mathbf{r}_{ij} - \mathbf{r}) \mathbf{F}_{ij} \mathbf{r}_{ij}}{\sum_i \sum_{j>i} \Theta(\langle N_{ij}(1)\rangle - N_{\mathrm{c}})} \tag{21}$$

where $\langle N_{ij}(1)\rangle$ is the expected number of attached motors/crossliners from eqn. 7 for a concentration of 1, and $\Theta(N)$ is the Heaviside step function with $\Theta(0) \equiv 0$. The total virial anisotropy per filament is therefore

$$\Delta \mathrm{w}_{\mathrm{pair}}(\mathbf{r}) = \mathrm{w}_{\mathrm{pair},yy}(\mathbf{r}) - \mathrm{w}_{\mathrm{pair},xx}(\mathbf{r}) \tag{22}$$

and its corresponding anisotropy measure as shown in the figures

$$\Delta \mathrm{w}_{\mathrm{pair}}(y) = \int \Delta \mathrm{w}_{\mathrm{pair}}(\mathbf{r})\, \mathrm{d}x. \tag{23}$$

Note that this anisotropy measure is independent of filament orientations because summing over the simulation-calculated values of $\mathbf{F}_{ij}$ and N_{ij} integrates out any explicit orientational dependence on these quantities.

3.2 Reference frames and thresholding

In order to define a polar reference frame for unique comparison of minus-minus, plus-plus, and plus-minus steric interactions we considered the orientation of each filament $\hat{\mathbf{u}}_i$ and the instantaneous nematic director $\hat{\mathbf{n}}(t)$. To calculate $\hat{\mathbf{n}}(t)$, we first calculated the order parameter tensor $\mathbf{Q}(t)$, defined in 2D as

$$\mathbf{Q}(t) = \frac{2}{N} \sum_i^N \hat{\mathbf{u}}_i \hat{\mathbf{u}}_i - \mathbf{I} \tag{24}$$

where $\mathbf{I}$ is the identity matrix. The instantaneous nematic director $\hat{\mathbf{n}}(t)$ is then defined as the pseudovector corresponding to the maximum eigenvalue of $\mathbf{Q}(t)$. Since the nematic director is a pseudovector, we constrained $\hat{\mathbf{n}}(t)$ to lie in the northern hemisphere of the plane of the simulation. The instantaneous polar nematic director for filament i is then defined as

$$\hat{\mathbf{n}}_{\mathrm{p},i}(t) = \mathrm{sgn}\left(\hat{\mathbf{u}}_i(t) \cdot \hat{\mathbf{n}}(t)\right)\, \hat{\mathbf{n}}(t). \tag{25}$$

The frame given by $\hat{\mathbf{n}}_{\mathrm{p},i}(t)$ and the vector perpendicular to it $\left(\hat{\mathbf{n}}_{\mathrm{p},i}^{\perp}(t)\right)$ is used for all spatial measurements excluding motor densities. This reference frame distinguishes minus end-minus end interactions from plus end-plus end interactions for anti-polar pairs while.

All colormap data has been thresholded for clarity. Thresholds represented by the minimum (maximum) value are shown as the minimum (maximum) values on the colorbar associated with each density map. Values below (above) the thresholds are shown as the color representing the minimum (maximum) value on the associated colorbar. All colorbars are symmetric to ensure zero is always represented by the same color.

3.3 Motor density vs filament separation

To determine the motor density per filament as a function of filament separation y, we measured the average number density of motors attached to a filament pair at positions $(\mathbf{r}_i, \mathbf{r}_j)$ in the axis frame of each filament

$$n_{\mathrm{m}}(\mathbf{r}_{\mathrm{axis}}) = \frac{1}{2N} \left\langle \sum_i^N \sum_{j\neq i}^N N_{\mathrm{m},ij} \left[\delta\left(\left(\mathbf{r}_{ij}\cdot\hat{\mathbf{u}}_i^{\perp}\right)\hat{\mathbf{u}}_i^{\perp} + \left(\mathbf{r}_{ij}\cdot\hat{\mathbf{u}}_i\right)\hat{\mathbf{u}}_i - \mathbf{r}_{\mathrm{axis}}\right)\right] \right\rangle \tag{26}$$

where N is the total number of filaments, $N_{\mathrm{m},ij}$ is the number of motors linking filament i to filament j, $\hat{\mathbf{u}}_i$ is the vector along the filament i, $\hat{\mathbf{u}}_i^{\perp}$ is the vector perpendicular to the filament i, and $\mathbf{r}_{axis}$ is a vector in this axis frame for particle i defined by $(\hat{\mathbf{u}}_i^{\perp}, \hat{\mathbf{u}}_i)$. The factor of $1/2$ is to compensate for the double counting of the filament pairs. To determine this density as a function of filament separation y, we integrated out the perpendicular (x) contribution to the motor distribution function

$$n_{\mathrm{xl}}(y) = \frac{1}{2N} \int \left\langle \sum_i^N \sum_{j\neq i}^N N_{\mathrm{xl},ij} \left[\delta\left(\left(\mathbf{r}_{ij}\cdot\hat{\mathbf{u}}_i^{\perp}\right)\hat{\mathbf{u}}_i^{\perp} + \left(\mathbf{r}_{ij}\cdot\hat{\mathbf{u}}_i\right)\hat{\mathbf{u}}_i - \mathbf{r}_{\mathrm{axis}}\right)\right] \right\rangle \mathrm{d}x. \tag{27}$$

By integrating again along y, we obtain the total number of motors per filament

$$\int n_{\mathrm{xl}}(y)\, \mathrm{d}y = \frac{N_{\mathrm{xl}}}{N}. \tag{28}$$

4 Results

4.1 Comparison of equilibrium and motor-driven systems

In the absence of motors or crosslinkers, our system forms a 2D nematic liquid crystal phase in constant-volume simulations at the selected volume fraction (fig. S1a, S2, video S1) which serves as a useful reference state for understanding active stress generation. The stress produced arises solely from steric interactions between filaments resulting from their Brownian motion. When orientationally-aligned filaments undergo side-side steric interactions, the repulsion tends to separate the filaments perpendicular to the alignment direction, producing contractile stress (fig. 2b, left). End-end steric interactions tend to separate the filaments along the y direction, producing extensile stress (fig. 2b, right). As a result, the pairwise virial anisotropy density is positive (extensile) near $y = \pm 20$ due to end-end steric interactions and negative (contractile) near $y = 0$ (fig. 2c, S2). The contributions from different configurations integrate to zero, giving an isotropic stress tensor as required for an equilibrium system.

Motor activity drives extensile stress generation by altering filament interactions. The driven system is typically an active nematic phase with fluctuating polar lanes (fig. 3, S1b, video S2) characterized by extensile stress production and enhancement of

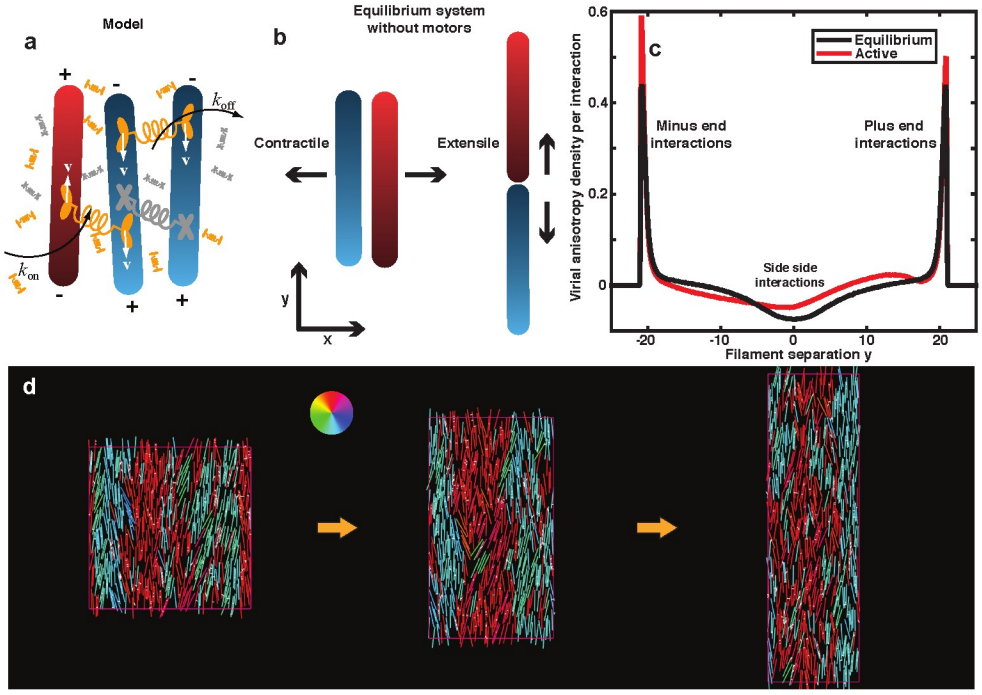

Fig. 2 Model and results overview. In schematics, lighter shading labels filament plus ends and color indicates filament plus-end orientation (red up, blue down, see color wheel in panel d). (a) Schematic of the model. Crosslinking motors (orange) and static crosslinkers (grey) bind and unbind; motors move toward filament plus ends. Filaments experience forces due to motors and crosslinkers, random thermal kicks, short-range steric repulsion, and drag from the solvent. (b) Schematic of steric interaction-induced stresses in an equilibrium system with no motors. Side-side steric interactions are contractile, while end-end steric interactions are extensile. (c) Virial anisotropy density per interaction for an equilibrium system (black) and an active system (red). Anisotropic stress is a function of y, the pair separation along the nematic director measured in the polar nematic frame. (d) Snapshots of a constant-pressure simulation of an active system driven by motors (video S3). The periodic simulation box elongates along the director (y direction), indicating generation of anisotropic extensile stress. Both equilibrium and active simulations have a filament packing fraction $\phi = 0.4157$, $N = 4000$ filaments, and filament aspect ratio $r = 20$. Active system has motor parameters stall force $f = 6.0$, concentration $c = 0.5$, inverse lifetime $k_{0,m} = 1.0$, run length $\ell = 0.64$, interaction range $R_c = 1/\sqrt{2}$, and Peclet number $Pe = 1.358$.

the extensile peaks near $y = \pm 20$ (fig. 2c). This occurs over a wide range of motor parameters (all systems shown in fig. 3 and for both anti-aligned and polar-aligned filament pairs[28]). The periodic box of a constant-pressure simulation elongates in y direction, a hallmark of extensile stress production (fig. 2d, video S3). Motors both alter steric interactions between filaments and directly produce forces themselves, with different effects on polar anti-aligned versus polar aligned pairs.

4.2 Motor-driven sliding enhances extensile interactions of anti-aligned filament pairs.

When we examine active stress generation by anti-aligned filament pairs, we find that minus end-minus end interactions are enhanced by motor-driven sliding, leading to a larger extensile peak; while plus end-plus end steric interactions produce slightly less extensile stress than at equilibrium (fig. 4a, b, peaks at $y = \pm 20$). Motor sliding drives filaments minus-end first through the system where they can interact with minus ends of other anti-aligned filaments (fig. 4a, video S4). This increases the stress produced by minus end-minus end steric interactions relative to an equilibrium system (fig. 4b, c). In fig. 4c, we show integrals of the virial anisotropy density to determine contributions for different filament separations. For the $y < -18$ region that includes the minus end-minus end peak, the extensile stress generated in the active system is approximately twice that in equilibrium. For the region with $y > 18$ corresponding to the plus end-plus end peak, there is a slight decrease.

Strikingly, in the sliding region $-18 < y < 18$, the contractile stress present in the equilibrium system nearly vanishes in the active system (fig. 4c, center). As discussed above (fig. 1a), when two filaments meet at their minus ends, motors initially cause contraction until the filaments are side-by-side, and then extension as the filaments slide apart (visible in fig. 4b as an oscillation in the purple curve). The motor density is about 20% higher on filaments in extending configurations versus contracting (fig. 4d). Therefore, motor driving adds additional forces that favor extension, making filament side-side interactions less contractile. Together these effects produce net extensile stress for anti-aligned filament pairs.

4.3 Nonequilibrium motor tether relaxation generates extensile stress on polar-aligned filament pairs.

On polar-aligned filament pairs, motors favor alignment of filament centers of mass but don't cause significant relative sliding of a pair (fig. 4e). Accordingly, we find that motors on polar-aligned pairs cause only slight changes in the steric interactions: steric stresses produced both by end-end and side-side steric interactions are both slightly increased compared to the equilibrium

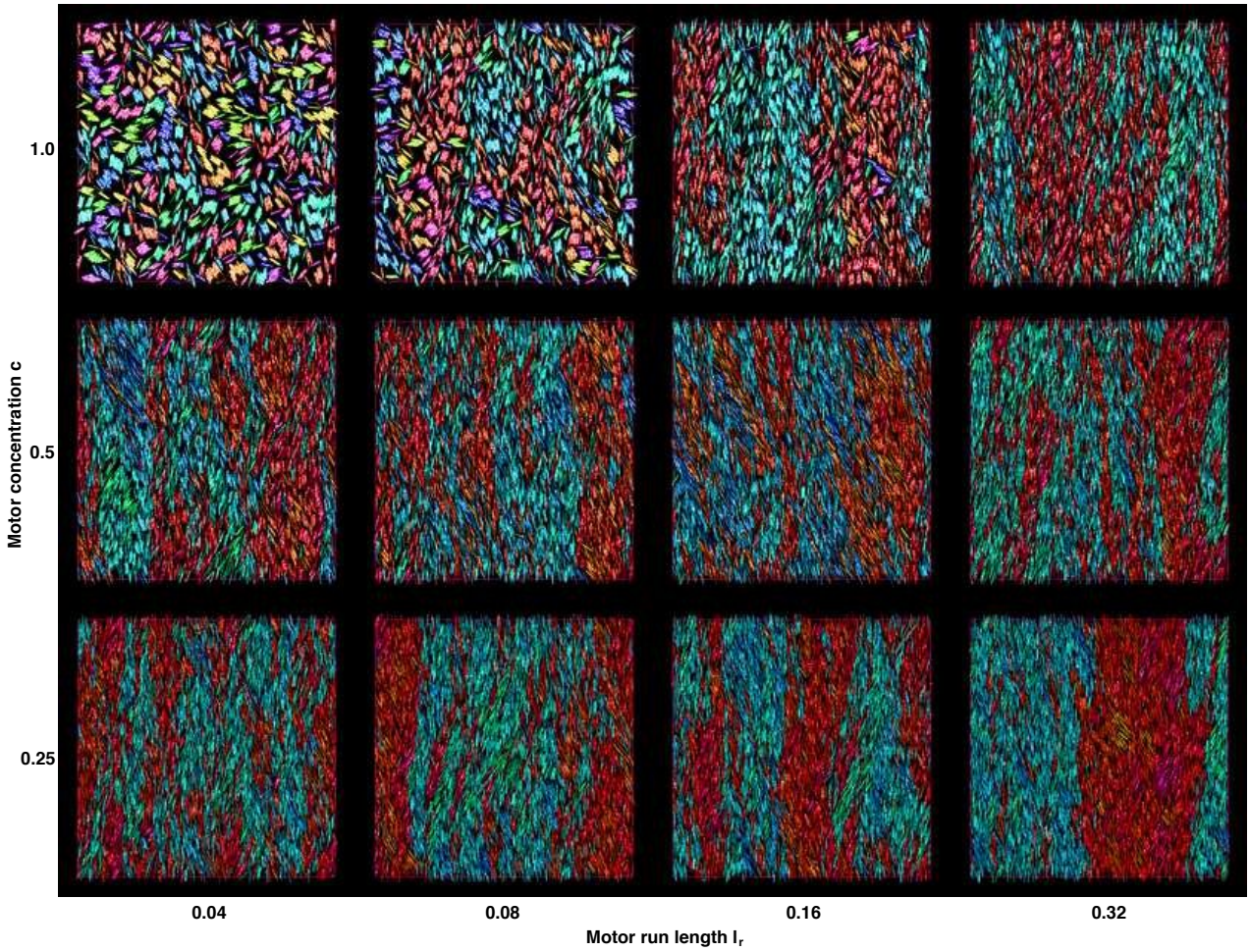

Fig. 3 Snapshot phase diagram with varying l_r and c. Other parameters found in table 2. An isotropic bundled state in which long, polar-aligned bundles are distributed with random orientation throughout the simulation box appears for high motor concentration and relatively small run length ($c = 1.0, l_r = 0.04,\ 0.08$). An active nematic state is much more prevalent, appearing for the majority of the parameter sets examined. The active nematic state contains large, generally short-lived polar domains with relatively few free anti-polar filaments within the domains.

system (fig. 4f, black versus cyan curves). However, motor forces cause a significant shift toward extensile stress production. The leading motor experiences an opposing force that slows it due to the motor force-velocity relation. This reduces the crosslink tether y extension and reduces the y component of the force exerted by the crosslink, decreasing filament pair contraction relative to a system with constant-speed motors (fig. 4e).

We can understand how this nonequilibrium tether relaxation alters force production in a mean-field model of fixed filaments. The motor number density $\psi(s_1, s_2)$ depends on filament arc length s_j ($j = 1, 2$) and evolves according to

$$\frac{\partial \psi}{\partial t} = -\frac{\partial (v_1 \psi)}{\partial s_1} - \frac{\partial (v_2 \psi)}{\partial s_2} + k_{\rm on} - k_{\rm off}\psi, \tag{29}$$

where v_j are the speeds of motor motion, $k_{\rm on}$ is the motor binding rate, and $k_{\rm off}$ is the unbinding rate. The motor binding kinetics are modeled as for the BD-kMC simulations (eqns. 5, 6), with the additional dimensional factor in the on rate that makes the binding rate is $k_{\rm on}(r) = \frac{k_0}{a^2} e^{-\beta u(r_c)}$, where a is a typical motor binding site size. For long parallel rods with aligned centers of mass, the steady-state motor distribution satisfies

$$0 = -\frac{\partial (v_1 \psi)}{\partial s_1} - \frac{\partial (v_2 \psi)}{\partial s_2} + \gamma e^{-\alpha (s_2 - s_1)^2} - k_{\rm off}\psi. \tag{30}$$

Here $\gamma = k_0 e^{\beta u_0 - \alpha d^2}/a^2$, where d is the perpendicular separation of the two rods, and $\alpha = \beta k/2$. In this case, the equation for ψ and the velocities are only functions of the motor extension parallel to the filament axes, $y_{\rm m} = s_2 - s_1$. Therefore we find an ODE in $y_{\rm m}$:

$$\frac{d(v_1 \psi)}{dy_{\rm m}} - \frac{d(v_2 \psi)}{dy_{\rm m}} + \gamma e^{-\alpha y_{\rm m}^2} - k_{\rm off}\psi = 0, \tag{31}$$

which is a first-order linear inhomogeneous ODE in ψ,

$$(v_2 - v_1)\psi' + (v_2' - v_1' + k_{\rm off})\psi = \gamma e^{-\alpha y_{\rm m}^2}. \tag{32}$$

where the primes denote differentiation with respect to $y_{\rm m}$.

If motors move at constant speed, $v_1 = v_2$ and $v_1' = v_2' = 0$, we recover the same Gaussian distribution as for static crosslinks (fig. 4g):

$$\psi_{st}(y_m) = \frac{\gamma}{k_{\rm off}} e^{-\alpha y_{\rm m}^2}. \tag{33}$$

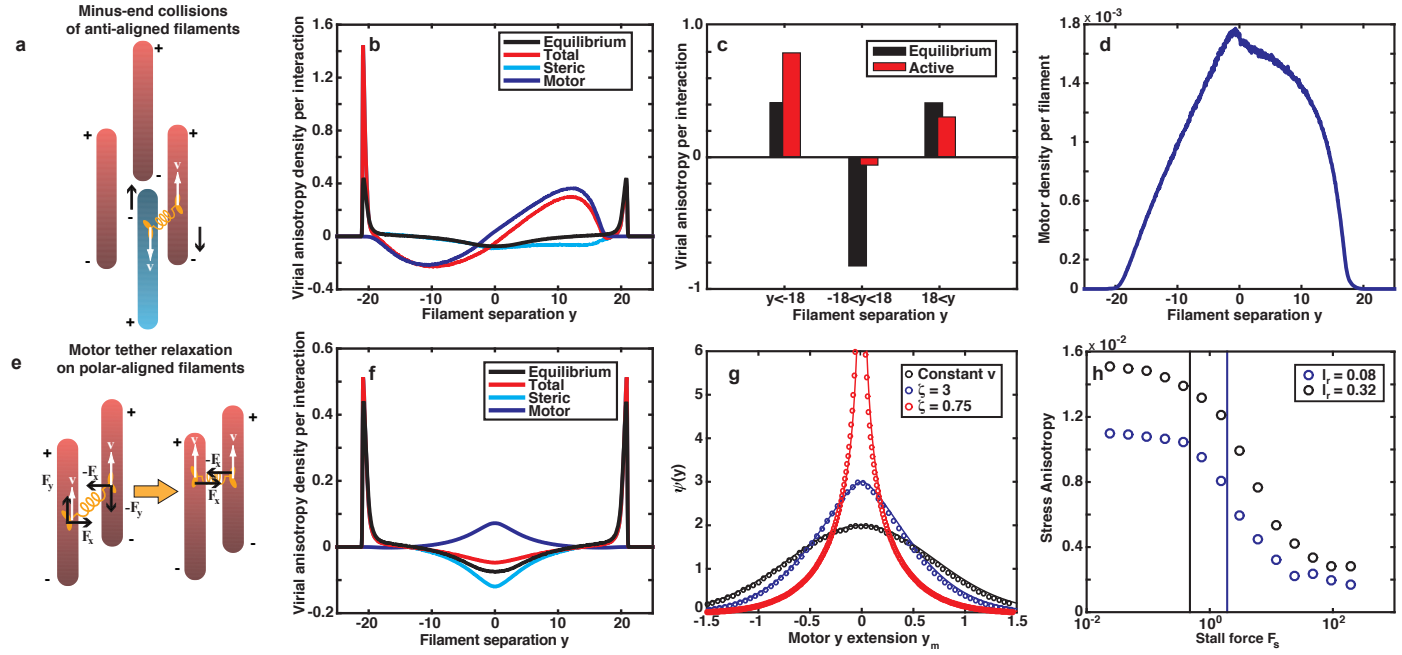

Fig. 4 Extensile stress generation by polar anti-aligned (top row) and polar-aligned (lower row) filament pairs. In schematics, lighter shading labels filament plus ends and color indicates filament plus-end orientation (red up, blue down). (a) Motor-driven sliding of anti-aligned filament pairs tends to increase steric interactions between filament minus ends and decrease steric interactions between filament plus ends. (b) Virial anisotropy density per interaction for anti-aligned pairs compared to an equilibrium system with no motors, as a function of y, the pair separation along the nematic director measured in the polar nematic frame. Black denotes the equilibrium reference system, red the total for the active system with motors, and cyan and purple the contributions from steric and motor forces, respectively. (c) Integrated virial anisotropy contributions (integrals of curves in panel b) for equilibrium and active systems. Black denotes the equilibrium reference system, red the total for the active system with motors. (d) Motor density as a function of filament separation for anti-aligned pairs. (e) Motors on polar-aligned filament pairs exert forces in the alignment direction (F_y) and perpendicular to the alignment direction (F_x) that tend to contract the filament pair (left). The larger opposing force on the leading motor slows its motion and makes the tether relax, reducing the y-direction forces (right). (f) Virial anisotropy density per interaction for polar-aligned pairs compared to an equilibrium system with no motors. (g) Distribution of motor y extension for motors moving on long fixed parallel filaments determined analytically (solid lines) and from simulations (points). Analytic curves were calculated using the dimensionless parameters $d=1$, $k=2$, $F_s=6$, $\beta=1$, $k_0=1$, $u_0=1+\ln 2$, $a=1$, and $v=0$ (constant speed curve), $v=1$ ($\zeta=3$ curve), $v=4$ ($\zeta=0.75$ curve). (h) Variation of extensile stress with stall force for systems of polar-aligned filaments. Vertical lines indicate stall force values for which $\zeta=1$. In simulations, unless otherwise noted both equilibrium and active simulations have a filament packing fraction $\phi=0.4157$, $N=4000$ filaments, and filament aspect ratio $r=20$. Active system has motor parameters stall force $f=6.0$, concentration $c=0.5$, inverse lifetime $k_{0,m}=1.0$, run length $\ell=0.64$, interaction range $R_c=1/\sqrt{2}$, and Peclet number $Pe=1.358$.

However, when motors instead move with a linear force-velocity relation, the distribution becomes more concentrated near zero extension and the shape is controlled by the parameter $\zeta = k_{\rm off}F_{\rm s}/(kv_0)$. In this case the motors move with a piecewise linear force-dependent velocity given by

$$v(F_\parallel) = \begin{cases} v_0, & F_\parallel \geq 0 \\ v_0(1+F_\parallel/F_{\rm s}), & -F_{\rm s} < F_\parallel < 0 \\ 0, & F_\parallel \leq -F_{\rm s}. \end{cases} \tag{34}$$

The equation for ψ at steady state can be solved using an integrating factor method with the integration constant set by requiring that the solution go to zero as $|y_{\rm m}| \to \infty$. The solution is

$$\psi(y_{\rm m}) = \begin{cases} \frac{F_s\gamma}{2kv_0} E_{(\zeta+1)/2}(\alpha y_{\rm m}^2) & |y_{\rm m}| \leq F_s/k \\ \frac{\gamma\sqrt{\pi}e^{k_{\rm off}^2/(4\alpha v_0^2)}}{2v_0\sqrt{\alpha}} e^{k_{\rm off}|y_{\rm m}|/v_0}\left[1-\mathrm{erf}\left(\sqrt{\alpha}|y_{\rm m}|+\frac{k_{\rm off}}{2\sqrt{\alpha}v_0}\right)\right] & F_s/k < |y_{\rm m}|. \end{cases} \tag{35}$$

Here $\zeta = k_{\rm off}F_{\rm s}/(kv_0)$ and the exponential integral function $E_n(x) = \int_1^\infty e^{-xt}t^{-n}dt$. When ζ is large (slow motors or high stall force), the distribution is qualitatively similar to that of constant-speed motors. However when $\zeta \leq 1$ (fast motors or low stall force), the distribution develops an integrable singularity as $y_m \to 0$. This indicates a qualitative change in the motor distribution in which a large population of motors with zero y extension develops, significantly decreasing the y-direction contracting forces exerted on filaments. Our analytic results agree well with simulation results on fixed parallel rods for motor extension dis-

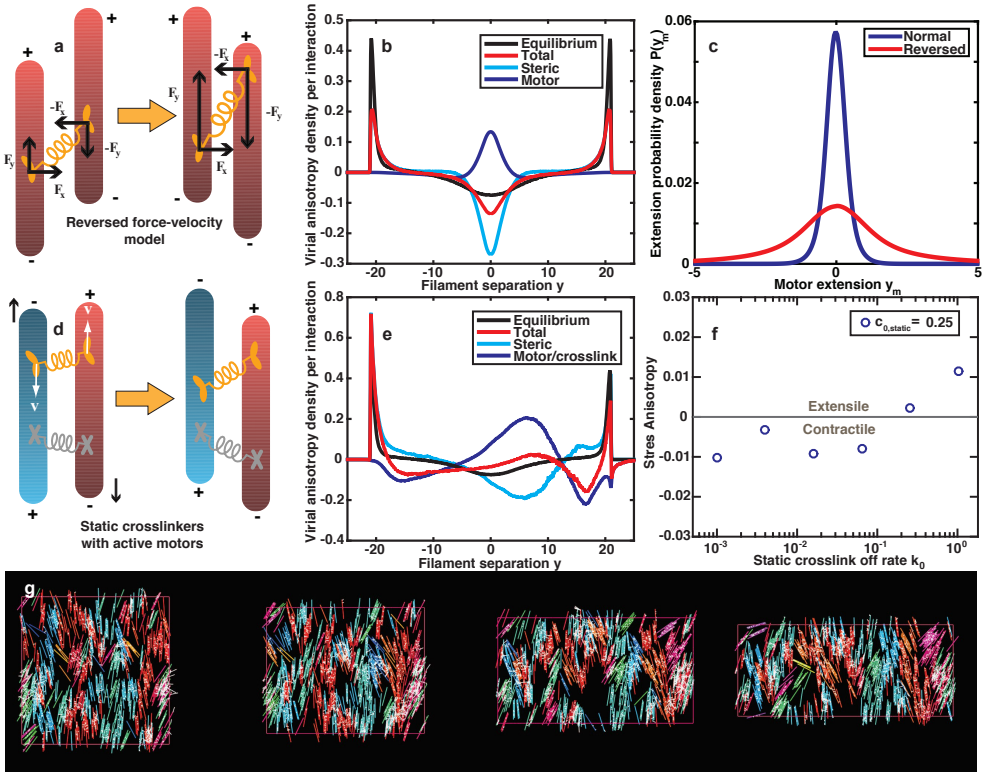

Fig. 5 Generation of active contractile stress in systems with altered motor force-velocity relation (top row) or static crosslinkers (lower two rows). In schematics, lighter shading labels filament plus ends and color indicates filament plus-end orientation (red up, blue down). (a) Schematic of reversed force-velocity relation model. Bound motors exert forces in the alignment direction (F_y) and perpendicular to the alignment direction (F_x) that tend to contract the filament pair (left). For motors with a reversed force-velocity relation, the larger opposing force on the leading motor increases its speed, increasing the motor tether extension and the y-direction forces (right). (b) Virial anisotropy density per interaction for the reversed force-velocity model compared to an equilibrium system with no motors, as a function of y, the pair separation along the nematic director measured in the polar nematic frame. Black denotes the equilibrium reference system, red the total for the system with reversed force-velocity motors, and cyan and purple the contributions from steric and motor forces, respectively. (c) Distribution of motor y extension for the reversed force-velocity model (red) compared to the conventional force-velocity model (blue). (d) Schematic of active system with static crosslinkers. Addition of static crosslinks partially gels the system, reducing filament sliding and causing motors to adopt configurations with increased tether extension. (e) Virial anisotropy density per interaction for the system with motors and static crosslinkers compared to an equilibrium system with no motors. Black denotes the equilibrium reference system, red the total for the system with motors and crosslnkers, and cyan and purple the contributions from steric and motor/crosslinker forces, respectively. (f) Anisotropic stress as a function of static crosslinker unbinding rate. (g) Snapshots of a constant-pressure simulation of a system with motors and static crosslinkers (video S8). The periodic simulation box is adjusted to produce constant pressure and elongates perpendicular to the director (x direction), indicating generation of contractile stress. Both equilibrium and active simulations have a filament packing fraction $\phi = 0.4157$, $N = 4000$ filaments, and filament aspect ratio $r = 20$. Active system has motor/crosslink parameters stall force $f = 6.0$, motor concentration $c = 0.5$, motor inverse lifetime $k_{0,m} = 1.0$, crosslink inverse lifetime $k_{0,c} = 0.01$, motor run length $\ell = 0.64$, motor/crosslink interaction range $R_c = 1/\sqrt{2}$, and motor Peclet number $Pe = 1.358$.

tributions away from the rod ends (fig. 4g).

The mean-field theory predicts that increasing the motor stall force will increase ζ and decrease nonequilibrium tether relaxation, thereby reducing extensile stress generation. We tested this in bulk simulations of moving polar-aligned filaments (all filament plus ends initially point in the same direction). As the stall force increases, we observe a transition to decreased extensile stress generation (fig. 4h). As expected, the crossover point occurs near $\zeta = 1$, showing that the mean-field theory qualitatively explains the change in extensile stress generation as a function of stall force. This comparison confirms that nonequilibrium crosslink tether relaxation is an important mechanism of extensile stress generation in our system.

4.4 Contractile stress production by altered motor kinetics or static crosslinkers

Based on our analysis of nonequilibrium motor tether relaxation, we predict that altering motor kinetics to increase motor tether y extension would produce contractile stress for polar-aligned filaments. We formulated a *reversed force-velocity model* in which the leading motor of a pair, which when experiencing a retarding force from the crosslink spring, *moves faster* than the trailing motor (fig. 5a, S1c, S4, video S5). This mechanism is related to Dasanayake and Carlsson's observation of increased motor extension in a simulation model of contractile actin-myosin gels[46]. While motor kinetics of this type have not been experimentally realized, this is a useful model to test our understanding of the role of filament steric interactions in stress generation. We find that although our system remains fluid, the reversed force-velocity mo-

tors lead to reduced extensile stress by end-end steric interactions and corresponding generation of contractile stress (fig. 5b, video S6). As expected, motor tethers become more extended in the y direction compared to the conventional force-velocity model (fig. 5c).

In actively-flowing nematic phases in the absence of static crosslinkers, we generically find extensile stress generation. A key contributor to extensile stress generation is the fluid nature of the material, in which motor activity enhances minus end-minus end steric interactions and decreases side-side steric interactions relative to an equilibrium nematic. Therefore, we expect that decreased fluidity will favor generation of contractile stress by decreasing filament end-end steric interactions and/or increasing filament side-side steric interactions. Indeed, the addition of long-lived static crosslinkers to our system (fig. 5d) favors contractile stress generation (fig. 5e-g, S1d, S5, videos S7, S8). While the system develops complex structure and virial anisotropy curves, we do find net contractile stress. Increasing the off rate of static crosslinkers increases fluidity and allows a transition back to extensile behavior (fig. 5f).

5 Conclusion

We used a 2D active nematic model of rigid filaments, crosslinking motors, and static crosslinkers to study mechanisms of active stress generation. Computing anisotropic stress density allowed us to determine the role of different filament configurations in stress generation. For an equilibrium system, filament end-end steric interactions produce extensile stress and side-side steric interactions produce contractile stress. These effects balance to give an overall isotropic stress tensor. In motor-driven systems, we typically find extensile stress generation: for polar anti-aligned filament pairs, motor-driven sliding enhances extensile minus end-minus end steric interactions and reduces contractile stress from side-side interactions. For polar-aligned filament pairs, sliding forces are relaxed when motors slow under a retarding force. This reduces motor tether extension and filament pair side-side contraction, thereby contributing to extensile stress generation. Based on our understanding of systems with crosslinking motors, we predicted alterations that would shift the system to contractile. Changing the motor force-velocity relation to increase sliding forces on polar-aligned filaments or adding long-lived static crosslinkers both lead to contractile stress generation.

While one-dimensional bundle contraction or expansion along the bundle axis and the bulk contraction or expansion may appear quite different, they are related: both require breaking the contraction/extension symmetry shown in fig. 1a, and similar mechanisms can lead to both bundle and bulk contraction[26]. A bundle or oriented system that extends along the bundle axis produces a dipolar stress tensor that drives flow of material out along the bundle axis and in perpendicular to the axis (fig. 1c). If such dipolar active stress occurs locally in an orientationally disordered system, particularly if motors or crosslinkers induce local filament alignment, it leads to bulk contraction (expansion) in all directions[26], corresponding to a positive isotropic pressure tensor. A similar connection exists for anisotropic contractile stress and bulk contraction. The same microscopic mechanisms can thus act in both types of systems.

Our work suggests that the balance between end-end and side-side steric interactions and the nature of motor- and crosslink-induced forces are determinants of extensile versus contractile stress generation in nematic motor-filament systems. In our simulations, extensile stress is typical for actively flowing motor-filament mixtures, as observed experimentally for reconstituted microtubule-kinesin mixtures[10,13,14], while contractile stress is typical for less-fluid systems with long-lived static crosslinkers, as occurs for reconstituted actin-myosin bundles[8,9,15,16]. This suggests that the differing fluidities of microtubule-kinesin versus actin-myosin systems may contribute to their differences in active stress generation.

Could the tuning of steric interactions and fluidity by motors and crosslinkers we describe be important in actin-myosin systems? Our assumption of rigid filaments makes the model most relevant to microtubules, which have persistence lengths of millimeters[1]. Actin filaments are more flexible, and their buckling is established to be important for actomyosin contractility,[7,15,47,48] making our model not directly relevant to actin-myosin systems. Actin-myosin systems often exhibit negative isotropic pressure, commonly referred to as contractility (in contrast to the dipolar contractile stress described here.) Multiple microscopic mechanisms have been proposed as important to actin-myosin contractility, including nonzero motor size, crosslink tether elasticity, spatially-varying motor motion, and filament buckling[5,7,15,26,46,47,49,50]. However, the motor- and crosslink-modulated alterations in steric interactions we describe could also occur for actin filaments and may complement effects of buckling in actomyosin gels.

Some experiments have observed that a minimum concentration of static crosslinkers is necessary for contractility in actin-myosin systems[5,12,51,52], consistent with our proposal that crosslink-induced gelation favors contractile stress generation. However, other experiments see contractility in the absence of static crosslinkers,[53–55] demonstrating that static crosslinkers are not required for actomyosin contractility. Even in these systems, it appears that a minimum myosin density is necessary to provide sufficient crosslinking for contractility.[50,54] The multiple myosin motors present in a single myosin filament and their tug-of-war dynamics may allow some fraction of the myosin motors to play the physical role of static crosslinkers in our model. Consistent with our model results, it does appear that sufficient crosslinking to form an actomyosin gel is important for contractility. In future work, it would be of interest to consider extensions to our model that would make it relevant to experimental actin-myosin systems, including longer filaments, filament flexibility, and varying density.

Acknowledgements. We thank J. Richard McIntosh for useful discussions. This work was funded by NSF grants EF-ATB-1137822 (MB), DMR-0847685 (MB), and DMR-0820579 (MG); NIH grant R01 GM104976-03 (MB); and the use of the Janus supercomputer supported by NSF grant CNS-0821794.

Author contributions. RB, MG, and MB formulated the models, RB, OS, CB, and MG wrote the simulation code, RB ran simulations, RB, LH, MG, and MB analyzed the results, RB and MB

formulated and analyzed the mean-field theory, MG and MB supervised the project, and RB, LH, and MB wrote the paper.

The authors declare that they have no competing financial interests.

Correspondence and requests for materials should be addressed to mdb@colorado.edu.

References

1 D. Bray, *Cell movements: from molecules to motility*, Routledge, 2000.

2 F. Nedelec, T. Surrey, A. C. Maggs and S. Leibler, *Nature*, 1997, **389**, 305–308.

3 T. Surrey, F. Nédélec, S. Leibler and E. Karsenti, *Science*, 2001, **292**, 1167–1171.

4 F. Backouche, L. Haviv, D. Groswasser and A. Bernheim-Groswasser, *Physical Biology*, 2006, **3**, 264.

5 P. M. Bendix, G. H. Koenderink, D. Cuvelier, Z. Dogic, B. N. Koeleman, W. M. Brieher, C. M. Field, L. Mahadevan and D. A. Weitz, *Biophysical Journal*, 2008, **94**, 3126–3136.

6 V. Schaller, C. Weber, C. Semmrich, E. Frey and A. R. Bausch, *Nature*, 2010, **467**, 73–77.

7 M. S. e. Silva, M. Depken, B. Stuhrmann, M. Korsten, F. C. MacKintosh and G. H. Koenderink, *Proceedings of the National Academy of Sciences*, 2011, **108**, 9408–9413.

8 M. P. Murrell and M. L. Gardel, *Proceedings of the National Academy of Sciences*, 2012, **109**, 20820–20825.

9 A.-C. Reymann, R. Boujemaa-Paterski, J.-L. Martiel, C. Guérin, W. Cao, H. F. Chin, E. M. D. L. Cruz, M. Théry and L. Blanchoin, *Science*, 2012, **336**, 1310–1314.

10 T. Sanchez, D. T. N. Chen, S. J. DeCamp, M. Heymann and Z. Dogic, *Nature*, 2012, **491**, 431–434.

11 M. R. Stachowiak, P. M. McCall, T. Thoresen, H. E. Balcioglu, L. Kasiewicz, M. L. Gardel and B. O'Shaughnessy, *Biophysical Journal*, 2012, **103**, 1265–1274.

12 Y. Ideses, A. Sonn-Segev, Y. Roichman and A. Bernheim-Groswasser, *Soft Matter*, 2013, **9**, 7127–7137.

13 G. Henkin, S. J. DeCamp, D. T. N. Chen, T. Sanchez and Z. Dogic, *Philosophical Transactions of the Royal Society A: Mathematical, Physical and Engineering Sciences*, 2014, **372**, 20140142–20140142.

14 F. C. Keber, E. Loiseau, T. Sanchez, S. J. DeCamp, L. Giomi, M. J. Bowick, M. C. Marchetti, Z. Dogic and A. R. Bausch, *Science*, 2014, **345**, 1135–1139.

15 M. Lenz, T. Thoresen, M. L. Gardel and A. R. Dinner, *Physical Review Letters*, 2012, **108**, 238107.

16 N. Yoshinaga and P. Marcq, *Physical Biology*, 2012, **9**, 046004.

17 R. A. Simha and S. Ramaswamy, *Physica A: Statistical Mechanics and its Applications*, 2002, **306**, 262–269.

18 K. Kruse, J. Joanny, F. Jülicher, J. Prost and K. Sekimoto, *Physical Review Letters*, 2004, **92**, 078101.

19 F. MacKintosh and A. Levine, *Physical Review Letters*, 2008, **100**, 018104.

20 J.-F. Joanny and J. Prost, *HFSP Journal*, 2009, **3**, 94–104.

21 L. Giomi, M. J. Bowick, X. Ma and M. C. Marchetti, *Physical Review Letters*, 2013, **110**, 228101.

22 S. P. Thampi, R. Golestanian and J. M. Yeomans, *Physical Review Letters*, 2013, **111**, 118101.

23 J. R. Mcintosh, P. K. Hepler and D. G. V. Wie, *Nature*, 1969, **224**, 659–663.

24 K. Kruse and F. Jülicher, *Physical Review Letters*, 2000, **85**, 1778–1781.

25 T. B. Liverpool and M. C. Marchetti, *EPL (Europhysics Letters)*, 2005, **69**, 846.

26 M. Lenz, *Physical Review X*, 2014, **4**, 041002.

27 K. Kruse and K. Sekimoto, *Physical Review E*, 2002, **66**, 031904.

28 T. Gao, R. Blackwell, M. A. Glaser, M. Betterton and M. J. Shelley, *Physical Review Letters*, 2015, **114**, 048101.

29 A. Ahmadi, M. C. Marchetti and T. B. Liverpool, *Physical Review E*, 2006, **74**, 061913.

30 M. J. Schnitzer, K. Visscher and S. M. Block, *Nature Cell Biology*, 2000, **2**, 718–723.

31 M. T. Valentine, P. M. Fordyce, T. C. Krzysiak, S. P. Gilbert and S. M. Block, *Nature Cell Biology*, 2006, **8**, 470–476.

32 B. Guo and W. H. Guilford, *Proceedings of the National Academy of Sciences*, 2006, **103**, 9844–9849.

33 F. Nedelec and D. Foethke, *New Journal of Physics*, 2007, **9**, 427.

34 D. A. Head, G. Gompper and W. J. Briels, *Soft Matter*, 2011, **7**, 3116.

35 D. A. Head, W. J. Briels and G. Gompper, *Physical Review E*, 2014, **89**, 032705.

36 H. Lowen, *Physical Review E*, 1994, **50**, 1232–1242.

37 M. A. Bates and D. Frenkel, *The Journal of Chemical Physics*, 2000, **112**, 10034–10041.

38 P. Bolhuis and D. Frenkel, *Journal of Chemical Physics*, 1997, **106**, 666–687.

39 S. C. McGrother, D. C. Williamson and G. Jackson, *The Journal of Chemical Physics*, 1996, **104**, 6755–6771.

40 B. Alberts, A. Johnson, J. Lewis, M. Raff, K. Roberts and P. Walter, *Molecular Biology of the Cell*, Garland, New York, 5th edn., 2008.

41 D. Wirtz, *Annual Review of Biophysics*, 2009, **38**, 301–326.

42 K. Visscher, M. J. Schnitzer and S. M. Block, *Nature*, 1999, **400**, 184–189.

43 C. M. Coppin, J. T. Finer, J. A. Spudich and R. D. Vale, *Biophysical Journal*, 1995, **68**, 242S–244S.

44 D. Frenkel and B. Smit, *Understanding molecular simulation: from algorithms to applications*, Academic press, 2001, vol. 1.

45 J. F. Brady, *The Journal of Chemical Physics*, 1993, **98**, 3335–3341.

46 N. L. Dasanayake and A. E. Carlsson, *Physical Biology*, 2013, **10**, 036006.

47 M. Lenz, M. L. Gardel and A. R. Dinner, *New Journal of Physics*, 2012, **14**, 033037.

48 A. Córdoba, J. D. Schieber and T. Indei, *Soft Matter*, 2014.

49 D. Gordon, A. Bernheim-Groswasser, C. Keasar and O. Farago,

Physical Biology, 2012, **9**, 026005.

50 S. Wang and P. G. Wolynes, *Proceedings of the National Academy of Sciences*, 2012, **109**, 6446–6451.

51 S. Köhler and A. R. Bausch, *PLoS ONE*, 2012, **7**, e39869.

52 V. Schaller, B. Hammerich and A. R. Bausch, *The European Physical Journal E*, 2012, **35**, year.

53 Y. Tanaka-Takiguchi, T. Kakei, A. Tanimura, A. Takagi, M. Honda, H. Hotani and K. Takiguchi, *Journal of Molecular Biology*, 2004, **341**, 467–476.

54 T. Thoresen, M. Lenz and M. L. Gardel, *Biophysical Journal*, 2011, **100**, 2698–2705.

55 T. Thoresen, M. Lenz and M. L. Gardel, *Biophysical Journal*, 2013, **104**, 655–665.